



Photocatalytic oxidation of nitrogen monoxide and *o*-xylene by TiO₂/ZnO/Bi₂O₃ nanofibers: Optimization, kinetic modeling and mechanisms

Carina Chun Pei, Wallace Woon-Fong Leung*

Department of Mechanical Engineering, The Hong Kong Polytechnic University, Hung Hom, Hong Kong

ARTICLE INFO

Article history:

Received 19 September 2014
Received in revised form 9 March 2015
Accepted 13 March 2015
Available online 17 March 2015

Keywords:

TiO₂/ZnO/Bi₂O₃ composite nanofibers
Solar-light driven photocatalyst
Kinetic model
NO conversion
o-Xylene degradation

ABSTRACT

Semiconductor heterojunction structures can effectively enhance the separation efficiency of photogenerated electron/hole pairs and the subsequent photocatalytic performance. With enhanced heterojunctions, novel TiO₂/ZnO/Bi₂O₃ composite nanofibers, synthesized by a simple sol-gel assisted electrospinning method, exhibited much higher photocatalytic activity for the oxidation of nitrogen monoxide (NO) under simulated solar irradiation than commercial TiO₂ nanoparticles. The composite nanofibers increased absorption in both UV and visible range when compared with TiO₂ nanoparticles. The enhanced photocatalytic activity of TiO₂/ZnO/Bi₂O₃ was attributed to the difference in the energy band positions of anatase, rutile, zincite and bismuth oxide, resulting in both lower band-gap energy and reduced recombination rate of photogenerated electron/hole pairs. Moreover, the photocatalytic performances were more stable for TZB nanofibers than that of TiO₂ nanoparticles, which were easily deactivated. In addition, a new kinetic model, taken into account of flow retention time and physical-chemical kinetics, was used to shed light on the behavior of the photocatalytic reaction. Faster kinetics (resulting in higher reactor throughput) and higher conversion efficiency of NO could be realized by optimizing the bismuth concentration in the composite nanofibers. The degradation pathway of *o*-xylene by TZB had also been investigated.

© 2015 Elsevier B.V. All rights reserved.

1. Introduction

Tremendous efforts have been put into developing highly effective photocatalysts for pollution abatement. As for the most studied photocatalyst, titanium dioxide suffers from low sunlight responsiveness (solar irradiation consisting of respectively, approximately 5% UV light, 43% visible light, and 52% harvestable infrared light); which defers its use for otherwise much wider industrial applications. Thus, designing, fabricating, and tailoring the physicochemical and optical properties of titanium dioxide to make use of a larger fraction of the solar spectrum is inevitable. Along this objective, TiO₂ is modified by various approaches, such as metal ion doped titanium dioxide [1–5]; non-metal ion doped titanium dioxide [6–8]; mixed phases titanium dioxide [9–11]; titanium dioxide coupled with other semiconductor [12–14] and sensitization of titanium dioxide with organic compounds/inorganic metal complexes [15,16].

In one approach that has been extensively studied, semiconductor heterojunction structures have been developed as an effective means to enhance the photogenerated electron/hole separation efficiency and the photocatalytic performance. The vectorial charge transfer from one semiconductor to another with suitable band edge positions that are thermodynamically favorable can increase the lifetime of the charge carriers thus promoting the interfacial charge transfer and improving the catalytic efficiency. On the other hand, TiO₂ composite is fabricated with narrow band-gap semiconductors to produce photocatalysts that can harvest visible light.

Among various narrow band-gap semiconductors such as CdS, WO₃ and Fe₂O₃, Bi₂O₃ has been widely investigated due to its small band gap (2.8 eV). Indeed, Bi₂O₃ has proven to be an efficient photocatalyst under visible-light irradiation. The intrinsic polarizability induced by the Bi 6s² lone pairs of electron is helpful for the separation of the photogenerated electron-hole pairs and the transfer of the charge carriers. In the literature, heterostructured photocatalysts, such as TiO₂/Bi₂O₃ [17,18] and ZnO/Bi₂O₃ [19] have been investigated. In particular, TiO₂/Bi₂O₃ composite photocatalyst can be easily activated by visible light

* Corresponding author. Tel.: +852 2766 6670; fax: +852 2365 4703.
E-mail address: wallace.leung@polyu.edu.hk (W.W.-F. Leung).

due to its photosensitization property. Since the valence band of Bi_2O_3 is lower than that of TiO_2 , the $\text{TiO}_2/\text{Bi}_2\text{O}_3$ heterojunctions are formed in the composite, which promote the photo-generated holes in Bi_2O_3 to be transferred to the upper lying valence bands of TiO_2 . Consequently, the valence band holes and hydroxyl radicals, produced via oxidation of adsorbed H_2O , or $\cdot\text{HO}^-$, can degrade organic dyes under visible-light irradiation for the $\text{TiO}_2/\text{Bi}_2\text{O}_3$ composite nanoparticles [17]. Swaminathan et al. [19] have also studied the heterostructured $\text{Bi}_2\text{O}_3/\text{ZnO}$, which has increased UV absorption when compared with just ZnO by itself. The enhanced photocatalytic activity of $\text{Bi}_2\text{O}_3/\text{ZnO}$ is attributed to the low recombination rate of photo-induced electron–hole pairs, caused by the transfer of electrons and holes between ZnO and Bi_2O_3 . Despite of these efforts, the characteristics and photocatalysis from the heterostructured $\text{TiO}_2/\text{ZnO}/\text{Bi}_2\text{O}_3$, that might have better synergistic properties, have yet been investigated.

Electrospinning is a commonly used fabrication technique for fabricating continuous nanofibers from a wide range of materials with diameters in the range of several nanometers to micrometers. It can be considered as a low-cost and effective method to synthesize composite photocatalyst in nanosize. Therefore, in this study, $\text{TiO}_2/\text{ZnO}/\text{Bi}_2\text{O}_3$ composite nanofibers are fabricated through a sol–gel assisted electrospinning method and the photocatalytic efficiency is monitored based on oxidation of nitrogen monoxide (NO), which is one of the major contributors to acid rain and urban smog. In addition, a new kinetic model taken into account of both flow retention time and kinetics (chemical and physical) has been developed to quantify the behavior of the photocatalytic reaction. Lastly, the degradation pathway of *o*-xylene as a representative volatile organic compound (VOC) using TZB has been investigated.

2. Methodology

2.1. Materials

Titanium tetraisopropoxide (TIIP), zinc acetate dehydrate, bismuth(III) nitrate pentahydrate, polyvinyl pyrrolidone (PVP) (MW=36,000), isometric acetic acid and benchmark test TiO_2 nanoparticles (Degussa P25) were all purchased from Sigma–Aldrich, while ethanol was purchased from Advanced Technology & Industrial Company. All reagents were of analytical grade and used without any further purification.

2.2. Fabrication

Composite nanofibers made of $\text{TiO}_2/\text{ZnO}/\text{Bi}_2\text{O}_3$ (abbreviated as TZB) could be produced based on a sol–gel method. First, 3% (V/V) TIIP and isometric acetic acid were mixed with 4% (w/w) PVP powders and ethanol. The mixture was under ultrasonication for 30 min. Subsequently, 0.1% zinc acetate dehydrate and a portion of bismuth (III) nitrate pentahydrate was added to the solution with sufficient mixing (under ultrasonication) for 6 h to obtain a homogeneous solution to be fed to the nozzle-less electrospinning device. A thin film of solution was conveyed out of the liquid pool by the rotating electrode. Under the electric field, a jet was produced from instability due to the surface tension at the liquid surface being overtaken by the electric field force acting between the positively charged rotating electrode and the ground collector. The fibers jetted into the air, and positive charges deposited on the fiber repelled against each other, and together with evaporation, the diameter of the fibers reduced continuously during the free flight of the fibers from the rotating electrode to the ground collector. The collected electrospun fibers were subsequently calcinated in a furnace with temperature ramping slowly to 650°C

(at heating rate of 1°C min^{-1}). Under controlled evaporation, both organic compounds (e.g., ethanol, PVP) and residual water left in the nanofibers were slowly removed.

2.3. Characterization

The thermal decomposition behavior of precursor xerogel was examined using a thermo gravimetric analyzer and differential scanning calorimeter (TGA–DSC) (Netzsch) under ambient pressure in the temperature range between 50 and 650°C at a controlled heating rate of $10^\circ\text{C min}^{-1}$.

The morphologies of nanofibers were investigated using scanning electron microscope with energy dispersive spectroscopy (SEM–EDS) (JEOL Model JSM-6490) and transmission electron microscopy (TEM) (JEOL Model JEM-2011).

Phase analyses were carried out on X-ray diffraction (XRD) (Rigaku SmartLab) in the range of 20 – 80° (2θ) at ambient condition.

The UV–vis diffuse reflectance spectra (DRS) were measured and recorded on a Varian Cary 100 Scan UV–vis system equipped with a Labsphere diffuse reflectance accessory to obtain the reflectance spectra of the catalysts over a range of 200–800 nm. BaSO_4 (Labsphere USRS-99-010) was used as a reference in the measurement. The measured spectra were converted from reflection to absorbance by the Kubelka–Munk equation.

Electrochemical impedance spectroscopy (EIS) measurement was carried out with a computer assisted potentiostat (Princeton 2273). The TZB film was peeled off from the glass slide after 2 h heat treatment and subsequently transferred to another FTO glass pre-coated with an ultra-thin adhesive layer of TiO_2 paste. The device for the EIS testing was obtained after it was calcinated again at 450°C for 2 h. The thickness was determined to be $20\text{ }\mu\text{m}$ from Surface Profilometer (Veeco Dektak 8) and the active area was 10 mm^2 . The AC perturbation signal applied in this test was 10 mV over the frequency range of 1 MHz to 100 mHz. The illumination condition was AM 1.5 spectrum illumination with an incident power density of 100 mW cm^{-2} under temperature of 298 K. In the case of dark condition, EIS measurements were carried out without light but with the same bias voltage as that under illumination.

Specific surface areas were examined by the Brunauer–Emmett–Teller (BET) using N_2 adsorption at 77 K using Beckman Coulter SATM 3100.

2.4. Photocatalytic measurement

The photocatalytic efficiency of the composite TZB nanofibers was evaluated by the conversion of nitrogen monoxide (NO) and the degradation of *o*-xylene. Catalyst was placed in the center of a rectangular reactor ($10 \times 30 \times 15\text{ cm}^3$ $H \times L \times W$). A 300 W commercial tungsten halogen lamp (General Electric) was used as the simulated solar light source, which was vertically positioned above the sample dish outside the reactor. The initial concentration of NO was diluted to about 1000 ppb by the air stream supplied with a zero air generator (Thermo Environmental Inc., Model 111). The gas streams were premixed completely by a gas mixer, and the flow rate was controlled at 3 L min^{-1} by a mass flow controller. The concentration of NO was continuously measured by a chemiluminescence NO analyzer (Thermo Environmental Instruments Inc., Model 42c). The removal rate (%) of NO was calculated from the concentration of NO, respectively, in the feed and outlet streams. The detailed setup of the photocatalytic reaction has been illustrated in our previous study [20]. For the *o*-xylene test, pre-cleaned Summa canisters were evacuated for volatile organic compounds (VOCs) sampling. Constant VOC sampling time was achieved using a mass flow controller. Samples of VOC were collected at designated times during the experiment. After collection, the canister sample was first concentrated by a Nutech Cryogenic Concentrator (Model 3550A), and

the trapped VOC was separated and analyzed by Hewlett Packard Gas Chromatograph (Model HP 6890) and quantified by a Mass Selective Detector (Model HP 5973). After analysis, the canister was sequentially evacuated and pressurized with humidified zero air until all compounds were purged with level detected smaller than 0.2 ppb.

3. Results and discussion

3.1. Optimization of $\text{TiO}_2/\text{ZnO}/\text{Bi}_2\text{O}_3$ composite nanofibers

The TGA–DSC curve is shown in Fig. 1. Four distinct stages of loss in mass and change in heat flux can be identified in the TGA–DSC curve. The first stage is between 50 and 200 °C with a broad peak in the DSC curve indicating the loss of solvent (such as ethanol) in the composite sol. In the second stage with temperature between 200 and 400 °C, there is a sharp exothermic peak at about 375 °C, which is due to decomposition of the side chains of PVP, acetate, nitrate, titanate, and the by-products, such as isopropanol. In the third stage with temperature between 400 and 600 °C, an exothermic peak appeared in the TGA–DSC curve at about 500 °C, which is attributed to the degradation of the main chain of PVP, and the phase transitions of TiO_2 , ZnO and Bi_2O_3 . Both the

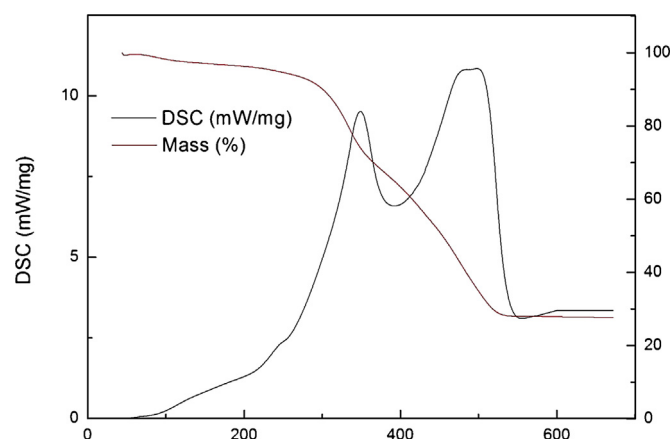


Fig. 1. TGA–DSC curve of the as-spun fibers.

TGA and DSC outputs were stabilized after reaching 600 °C, which indicated all the organic compounds had been removed. Thus, the calcination temperature of these composite nanofibers was set at 650 °C.

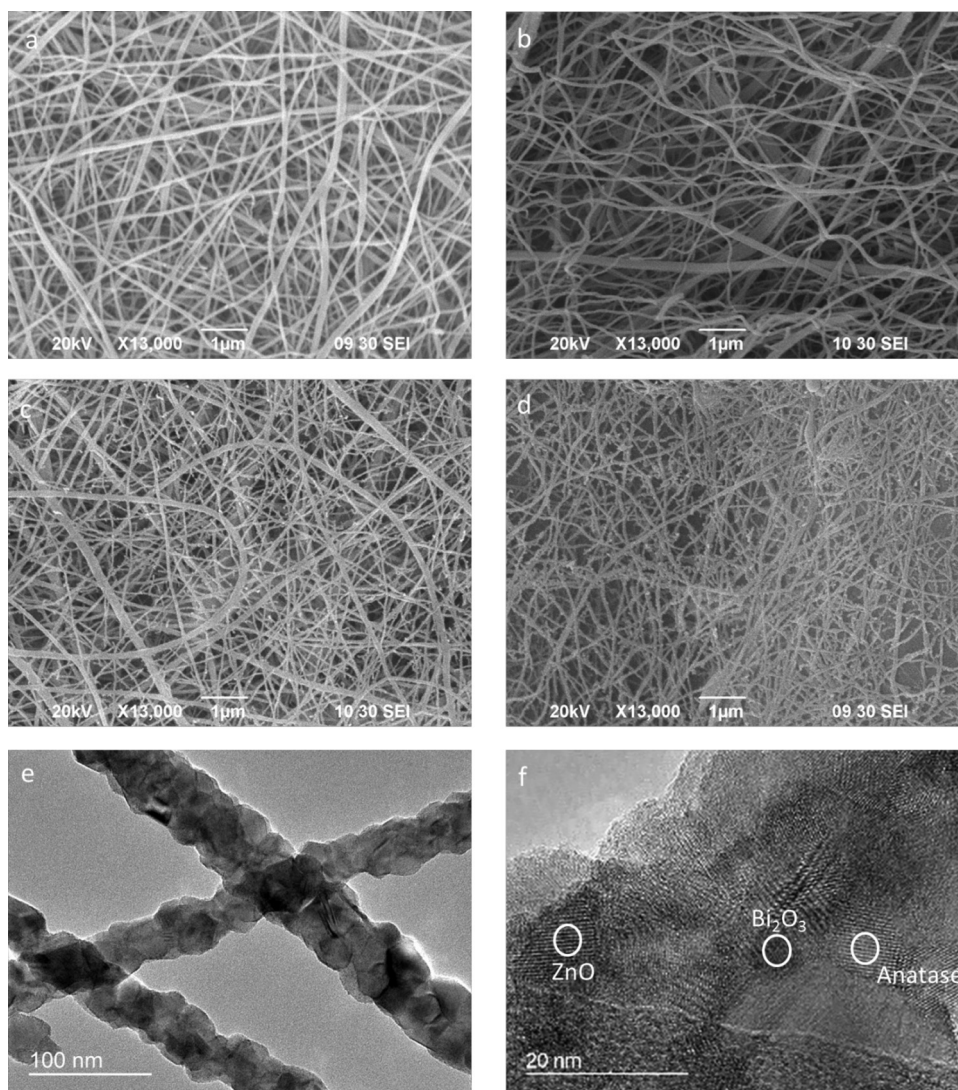


Fig. 2. SEM and TEM images of $\text{TiO}_2/\text{ZnO}/\text{Bi}_2\text{O}_3$ (TZB) nanofibers after calcination with different bismuth (III) nitrate pentahydrate concentrations in precursor solutions: a. 0.1%; b. 0.2%; c. 0.3%; d. 0.4%. e. TEM image of the prepared nanofibers (0.2%); f. HRTEM image of the fibers (0.2%).

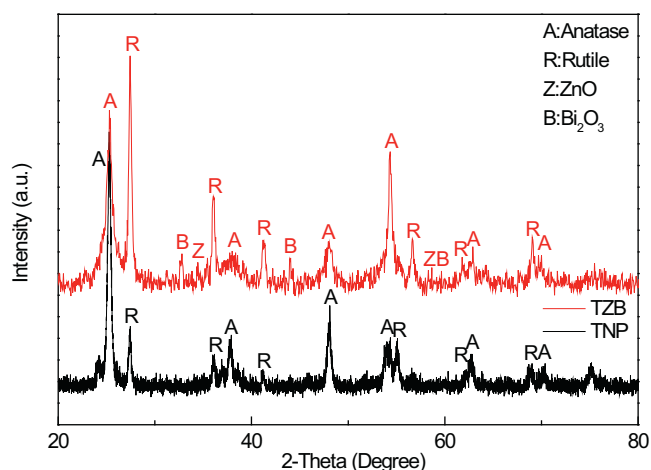


Fig. 3. XRD patterns of TZB composite nanofibers and commercial TiO_2 nanoparticles.

The morphology of the nanofibers was analyzed by SEM and TEM. Upon calcination, the nanofibers prepared with different Bi concentrations (0.1%, 0.2%, 0.3% and 0.4% in a–d, respectively) in the precursor solution are shown by the SEM pictures in Fig. 2. As can be seen, fine fibers are distributed randomly in layers. When the Bi concentration is at 0.1% and 0.2%, the fibers appear smooth and uniform. For higher Bi concentration up to 0.3% and 0.4%, some branch-like nanofibers are formed, which is due to the difference in the coefficients of thermal expansion among these three which are $9 \times 10^{-6} \text{ K}^{-1}$ (TiO_2), $4.75 \times 10^{-6} \text{ K}^{-1}$ (ZnO), and $18 \times 10^{-6} \text{ K}^{-1}$ (Bi_2O_3), respectively [21,22]. Under a higher bismuth concentration, the composite fibers are broken up into short rods because of strong thermal shock and shrinkage during the initial stage. When the temperature exceeds the softening point of PVP, these short rods will shrink. At higher temperature, all rods begin to melt partially, or fully; and subsequently re-bond with each other forming branch-like fibers [23,24]. From the SEM picture of 0.2% nanofibers (Fig. 2b), the average diameter of the nanofibers is about 90 nm, which agrees with the TEM picture depicted in Fig. 2e. The TEM picture also reveals the internal structure of the composite nanofibers, which are packed with nanocrystals. This unique structure provides nanopores between the nanocrystals, which are favorable for photocatalytic reaction. The HRTEM in Fig. 2f displays the lattice spacing of 3.52 Å, 2.81 Å, and 3.31 Å, which correspond to the crystal structure of anatase, zincite and bismuth oxide, respectively.

The XRD pattern of calcinated nanofibers and commercial TiO_2 nanoparticles are shown in Fig. 3. It reveals the presence of anatase (JCPDS card No. 21-1272), rutile (JCPDS card No. 21-1276), zincite (JCPDS card No. 65-682) and bismuth oxide (JCPDS card No. 41-1449) in the nanofiber composite, which is in accord with the HRTEM image in Fig. 2f.

The diffuse reflectance UV–vis spectra of both TZB nanofibers and commercial TiO_2 nanoparticles are compared in Fig. 4a. From the absorption spectra between 200 and 700 nm, the absorbance of TZB nanofibers in the UV range have been significantly improved when compared with TiO_2 nanoparticles, and the absorption edges have been shifted to the visible region. The samples with different contents of Bi show no difference in behavior in the UV range. For a crystalline semiconductor, the optical absorption near the band edge is expressed by the formula

$$\alpha h\nu = A(h\nu - E_g)^{\frac{n}{2}} \quad (1)$$

where α , $h\nu$, E_g and A correspond to absorption coefficient, Planck constant, light frequency, band gap, and a constant, respectively. The parameter n depends on the characteristics of the transition

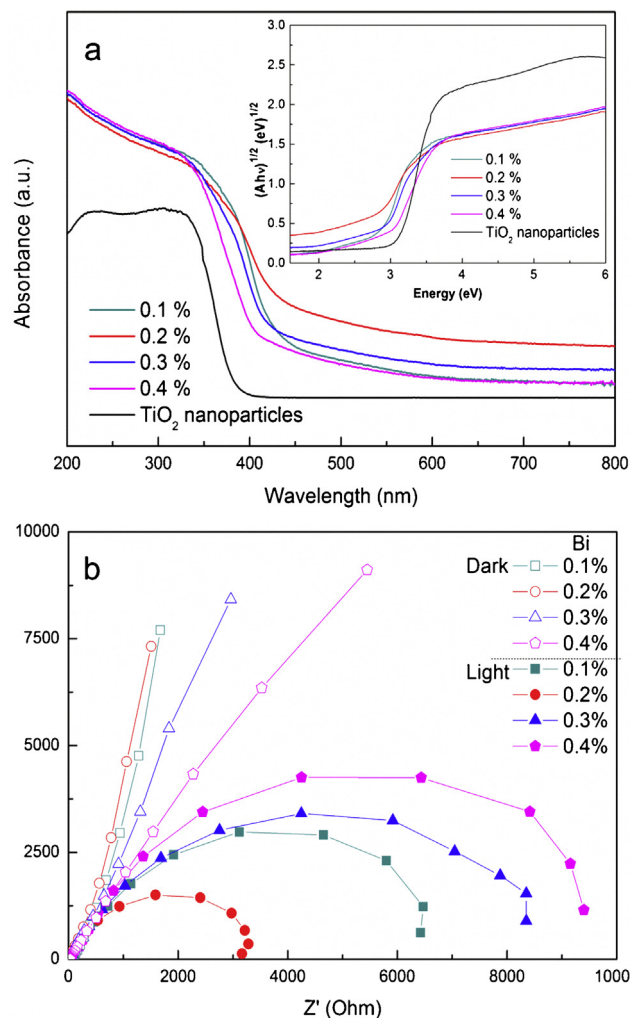


Fig. 4. (a) The UV–vis absorption spectra of TZB and commercial TiO_2 nanoparticles between 200 and 800 nm. The insert shows the UV–vis diffuse reflectance spectra (DRS) of from the Kubelka–Munk function versus the energy of light. (b) EIS changes of TZB nanofibers films with different bismuth (III) nitrate pentahydrate concentrations in dark and light conditions.

in a semiconductor; for a direct transition, $n = 1$, whereas for an indirect transition, $n = 4$. The absorption coefficient is proportional to the absorbance. For the composite photocatalyst, the transition is shown to be indirect. The band gap energy is estimated on the plot $(\alpha h\nu)^{1/2} = f(h\nu)$ by the intercept of the tangent to the plot with abscissa [25–27]. Using the Kubelka–Munk equation, the band gap of TZB nanofibers with Bi concentration 0.1%, 0.2%, 0.3% and 0.4% together with TiO_2 nanoparticles are determined to be 2.74 eV, 2.51 eV, 2.81 eV, 2.85 eV and 3.12 eV, respectively. The decrease in band-gap energy of TZB nanofibers as compared to TiO_2 nanoparticles can be attributed to the synergistic effect among anatase, rutile, ZnO , and Bi_2O_3 . The coupling of these semiconductors forms sub-bands in the forbidden band introducing impurities and defects, thereby reducing the band gap energy. Bi_2O_3 has the largest thermal expansion coefficient among TiO_2 , ZnO , and Bi_2O_3 , thus the lowest crystal bonding force. Therefore, when the Bi concentration increases, the composite fibers during annealing are broken up into short rods forming branch-like nanofibers at the crystal plane of Bi_2O_3 . The 0.2% Bi sample holds the lowest band gap which is attributed to the maximum heterojunctions [28–30].

As seen in Fig. 2f, ZnO and Bi_2O_3 dispersed on the surface of TiO_2 involved charge transfer between anatase and rutile due to the difference in their energy band positions during illumination.

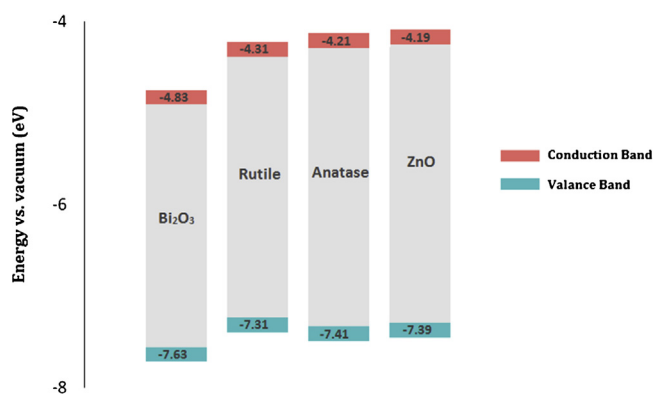


Fig. 5. Energy diagram of the composite TZB photocatalyst.

The TZB has an interesting energy diagram as shown in Fig. 5. This band position alignment favors movement of electrons and holes which facilitate generation of radicals with the water vapor in air, producing both oxygen and hydroxyl radicals.

The typical electrochemical impedance spectra are presented in Fig. 4b as Nyquist plots. Under dark condition, electrons transfer from conductive substrates (FTO glass) to the TZB film, and then diffuse through the film to the counter electrode. During the process of transmission, the electrons recombine in the electrolyte. The recombination process is the primary reaction at the interface under “dark condition”, which is detrimental for the photocatalytic process, thus it would be highly desirable to have high impedance under dark condition. The 0.2% Bi concentration reveals clearly the highest impedance among all. The coupling of different semiconductors can reduce the recombination rate, however, when Bi concentration is further increased, the excess Bi_2O_3 forms additional recombination centers. Thus, 0.2% Bi sample has the lowest recombination rate. Under illumination, the semicircle in the plot provides information on the charge transfer resistance which varies with different Bi concentrations. The 0.2% has the smallest semicircle, which indicated the least (i) solid-state interface layer resistance, and (ii) charge transfer resistance at the surface [31–33]. It benefits from the nanofiber morphology as well since samples with higher Bi concentration tend to break up forming nanorods. Overall, the 0.2% Bi concentration composite nanofibers has good electron acceptance and transport properties, as well as reduced charge recombination characteristic, thereby achieving higher rate of photocatalysis.

3.2. Photocatalytic oxidation of NO

Fig. 6 compares the NO removal rate as function of irradiation time for different TZB nanofiber samples (prepared under different dosages of bismuth (III) nitrate pentahydrate) and P25 TiO_2 nanoparticles. The tests were carried out under simulated solar-light irradiation with single-pass, flow-through reactor. After 30 min simulated solar-light irradiation, 37.5%, 67.2%, 20.5% and 17.1% of NO gas was oxidized by the TZB nanofibers prepared with Bi concentration of 0.1%, 0.2%, 0.3% and 0.4%, respectively; while a disappointing 8.5% of NO gas was oxidized by the P25 nanoparticles. Moreover, the NO removal rate increased rapidly in the first 5 min and ultimately reached the highest value and maintained constant thereafter for at least 30 min for TZB nanofibers. On the other hand, it took 15 min for TiO_2 nanoparticles to achieve the highest NO conversion of 8.5%, and subsequently the conversion rate decreased slowly to 6% at 30 min. The latter was ascribed to the accumulation of HNO_3 on the particles surface resulting in deactivation of photocatalyst. In general, the 0.2% TZB composite nanofibers reached the highest photocatalytic efficiency on the conversion of NO which can

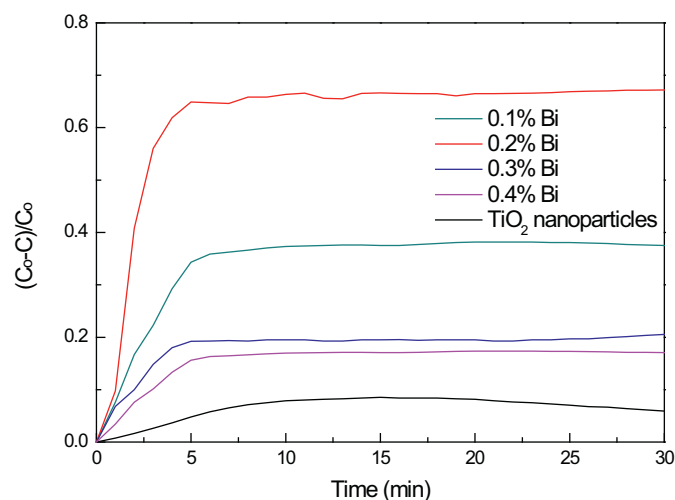


Fig. 6. The NO removal fraction against irradiation time in the presence of TZB nanofibers prepared for different Bi concentrations and for P25 (TiO_2 nanoparticles).

be explained by the highest solar light utilization, lowest band-gap energy, as well as the lowest electron–hole recombination rate.

3.3. Kinetic model

In this part, a new kinetic model is proposed to explain the behavior of the experimental data. In essence there are two time scales, one corresponding to the flow retention time t_R , i.e., the average time for which the pollutant gas resides in the reactor chamber; and the other time scale corresponding to the time scale for which physical/chemical process(es) take place in the reactor. For the latter, it is assumed that some time τ is required to realize the maximum pollutants conversion, or maximum sink capacity of pollutants. The typical time of the limiting process (physical/chemical) is assumed to be of order of this time scale τ . These two time-scales t_R and τ interact in a complicated way dictating the final outcome.

3.3.1. Kinetic time constant:

The time-limiting kinetics (or time to realize the maximum photo-oxidation capacity, i.e., sink capacity) can be attributed to:

- (a) Physical diffusion of pollutant gas and water vapor into the pores of the catalyst,
- (b) Adsorption of pollutant gas and water vapor onto the reactive site of the catalyst, and
- (c) The chemical reaction due to generation of the oxygen and hydroxyl radicals, valence band holes, and the chain of chemical reactions of these radicals and holes with the pollutant gas, converting it ultimately to harmless substances.

It is possible that the above three mechanisms may be limiting at various times during the reaction for which multiple time constants apply at various stages rather than having only one time constant being the dominant (i.e., longest time) for the entire process. This will be apparent later as τ is an assumed value in the model and it is determined from matching the experimental result with the model based on an assumed τ . The sketch of box model is given in Fig. S1.

It can be written

$$LA \frac{dC}{dt} = AU(C_a - C) - S^* \tanh\left(\frac{t}{\tau}\right) \quad (2a, b)$$

where

$$\tanh\left(\frac{t}{\tau}\right) = \frac{1 - \exp(-2t/\tau)}{1 + \exp(-2t/\tau)}$$

Eq. (2b) is an assumed form of the sink behavior and has a property such that at large $t \gg \tau$, $\tanh(t/\tau)$ approaches unity realizing the full oxidation capacity of the photocatalyst on the pollutants. It is convenient to define the following dimensionless variables:

$$\begin{aligned} C' &= \frac{C}{C_0} \\ t' &= \frac{Ut}{L} = \frac{t}{t_R} \\ \tau' &= \frac{\tau}{t_R} \\ S' &= \frac{S^*}{C_0AU} \end{aligned} \quad (3a-d)$$

where C_0 is the initial concentration of pollutant in the box, A is the cross sectional area of the box, and U is the through-flow velocity as determined from $U = Q/A$ with Q being the volumetric feed rate. Note τ' is the ratio of kinetic to retention time. When this ratio is much larger than unity, kinetics time is longer compared to the flow retention time in the reactor. On the other hand, when τ' is less than unity, flow condition (i.e., flow rate, chamber volume, etc.), rather than physical/chemical kinetics, controls the photocatalysis.

Dividing both sides by C_0AU , and with Eqs. (3a)–(3d), Eq. (2a) can be rewritten as,

$$\frac{dC'}{dt'} = (C'_a - C') - S' \tanh \frac{t'}{\tau'} \quad (4a)$$

Initial condition:

$$t' = 0, \quad C' \equiv \frac{C}{C_0} = 1 \quad (5a)$$

At “large” time:

$$t'/\tau' \gg 1$$

$$\frac{dC'}{dt'} \rightarrow 0 \quad \text{and} \quad \tanh \frac{t'}{\tau'} \quad (6b)$$

$$C'_a - C'_s - S' = 0$$

$$S' = C'_a - C'_s = 1 - C'_s$$

C'_s is the steady-state concentration. The first order differential equation Eq. (4a) can be integrated by the 4th-order Runge–Kutta algorithm. First, we rewrite Eq. (4a) as

$$\frac{dC'}{dt'} = f(t', C') = (C'_a - C') - S' \tanh \frac{t'}{\tau'} \quad (4b)$$

Using the Runge–Kutta algorithm,

$$\begin{aligned} k_1 &= f(t'_i, C'_i) = 1 - C'_i - S' \left[\frac{1 - \exp(-2t'_i/\tau')}{1 + \exp(-2t'_i/\tau')} \right] \\ k_2 &= f(t'_i + \Delta t/2, C'_i + k_1 \Delta t/2) = 1 - (C'_i + k_1 \Delta t/2) - S' \left[\frac{1 - \exp(-2[t'_i + \Delta t/2]/\tau')}{1 + \exp(-2[t'_i + \Delta t/2]/\tau')} \right] \\ k_3 &= f(t'_i + \Delta t/2, C'_i + k_2 \Delta t/2) = 1 - (C'_i + k_2 \Delta t/2) - S' \left[\frac{1 - \exp(-2[t'_i + \Delta t/2]/\tau')}{1 + \exp(-2[t'_i + \Delta t/2]/\tau')} \right] \\ k_4 &= f(t'_i + \Delta t, C'_i + k_3 \Delta t) = 1 - (C'_i + k_3 \Delta t) - S' \left[\frac{1 - \exp(-2[t'_i + \Delta t]/\tau')}{1 + \exp(-2[t'_i + \Delta t]/\tau')} \right] \\ C_{i+1} &= C_i + \frac{1}{6} \Delta t [k_1 + k_4 + 2k_2 + 2k_3] \end{aligned} \quad (6a-e)$$

The subscript “ i ” means the i th time step. The integration over time becomes a marching process starting from the initial condition at $i = 0$.

3.3.2. Instantaneous zero kinetic model

At times, the physical and chemical process governing the kinetics may happen so fast when compared to the flow retention time such that

$$\tau \ll t_R = \frac{L}{U} \quad \text{or} \quad \tau' = \frac{\tau U}{L} \ll 1$$

In this case, $\tau' \rightarrow 0$ for which $\tanh(t'/\tau') \rightarrow 1$, and Eq. (4a) reduces to

$$\frac{dC'}{dt'} \approx (C'_a - C') - S' \quad (4c)$$

Integrating Eq. (4c) with the initial condition Eq. (5a),

$$\begin{aligned} \tau' &< 1 \\ C' &= C'_s + (1 - C'_s) \exp(-t') \end{aligned} \quad (7)$$

Note that Eq. (7) does not have the kinetic time τ as it becomes redundant. Surely, as $t' \gg 1$, $C' \rightarrow C'_s$ as it should in Eq. (7). It turns out that as $\tau \leq 0.1$, the “full-blown” kinetic model, Eq. (4b), falls back to the instantaneous kinetic model. As such, Eq. (7) is also referred as the zero kinetic model, with $\tau' = 0$. When comparing the zero kinetic model with some test data showing slow kinetics, it is evident that the zero kinetic model, based on strictly flow retention time, cannot explain the slow kinetics of the test measurements, see Fig. 7a (compare the dotted curve with the test data). In other words, the conversion of NO gas is controlled by the kinetics of physical/chemical process and not controlled by the flow retention time (with the exception of the 0.2% Bi concentration which will be discussed later). Fig. 7a shows a better match between the kinetic model, using appropriate τ values, with experimental measurements at various Bi concentrations. The kinetic time τ is determined to be, respectively, $1.5 t_R$, $0.6 t_R$, $1.2 t_R$, and $1.4 t_R$ for Bi concentration of 0.1%, 0.2%, 0.3%, and 0.4%. In dimensional term, τ varies from 54 s to 135 s (given $t_R = L/U = V/Q = 1.5 \text{ min} = 90 \text{ s}$). This is the time scale to fully realize the maximum rate of photocatalytic oxidation. In Fig. 7b, the NO removal and kinetic time constants are plotted for different bismuth (III) nitrate pentahydrate concentrations. The 0.2% Bi not only has the maximum NO removal amount, it also has the fastest kinetics for the maximum removal; and these two parameters are inversely related. It is evident that the kinetic time for the 0.2% Bi concentration is only 0.6 of the flow retention time. This is also the only test case for which $\tau/t_R < 1$. This low ratio indicates that as soon as the NO gas is furnished to the reactor, conversion is almost instantaneous. As such, conversion depends on how fast the pollutant gas is furnished to the reactor (i.e., flow rate limited) and not by the kinetics. Further based on the test with different Bi concentrations in nanofibers all having similar morphology, it can be inferred that the diffusion and

convection of pollutant gas to the nanofibers are comparable. This means that the kinetics (if it becomes limiting) is probably due to chemical reaction and not by the physical process (diffusion or convection). For 0.3% Bi concentration, $\tau/t_R = 1.2$ which indicates that

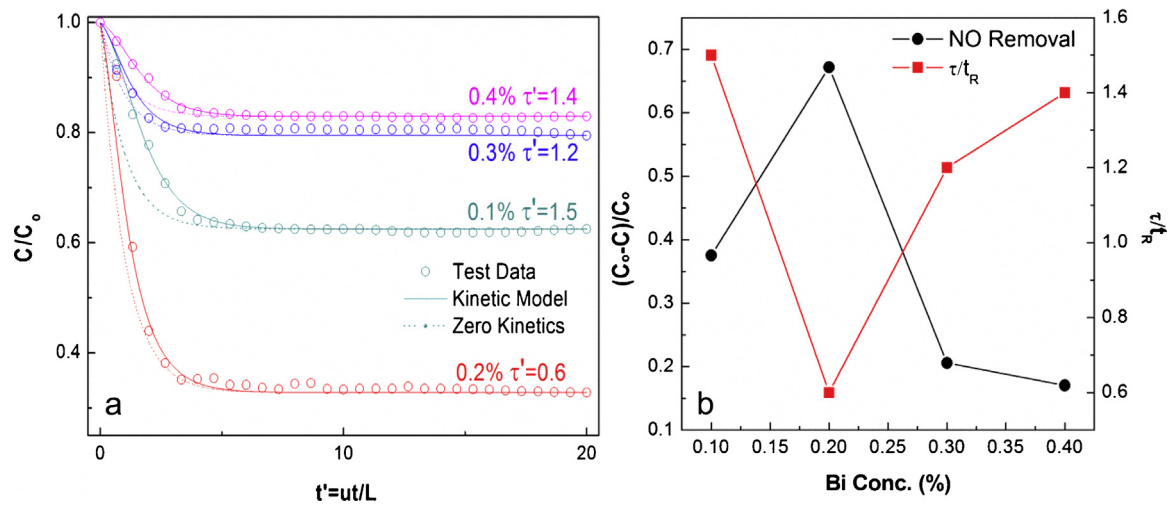


Fig. 7. (a) Comparing kinetic model prediction with actual performance of TZB photocatalysts; b. NO removal and kinetic time for different bismuth (III) nitrate pentahydrate concentrations.

the chemical kinetics time is twice as long as compared to that of 0.2% Bi concentration. Despite this given τ/t_R is not too much greater than unity, both kinetic and retention time are equally important.

It is rather reassuring that the 0.2% Bi concentration photocatalytic oxidation performance are also consistent with the characteristics of 0.2% Bi concentration that yields the highest light absorbance (Fig. 4a), highest electron–hole separation efficiency (i.e., least electron–hole recombination and highest impedance, see ordinate-scale in Fig. 4b), and highest charge carrier transport prop-

erties (see abscissa-scale in Fig. 4b) among all samples Bi = 0.1, 0.2, 0.3 and 0.4%, respectively.

3.4. Benchmark test

The benchmark test of TiO_2/ZnO (TZ) and $\text{TiO}_2/\text{Bi}_2\text{O}_3$ (TB) prepared by the same method has been carried out. Fig. 8a shows the XRD patterns of the synthesized TZ, TB and TZB nanofibers. The peaks corresponding to anatase, rutile, ZnO and Bi_2O_3 are identified according to the diffraction angles. The diffuse reflectance spectra

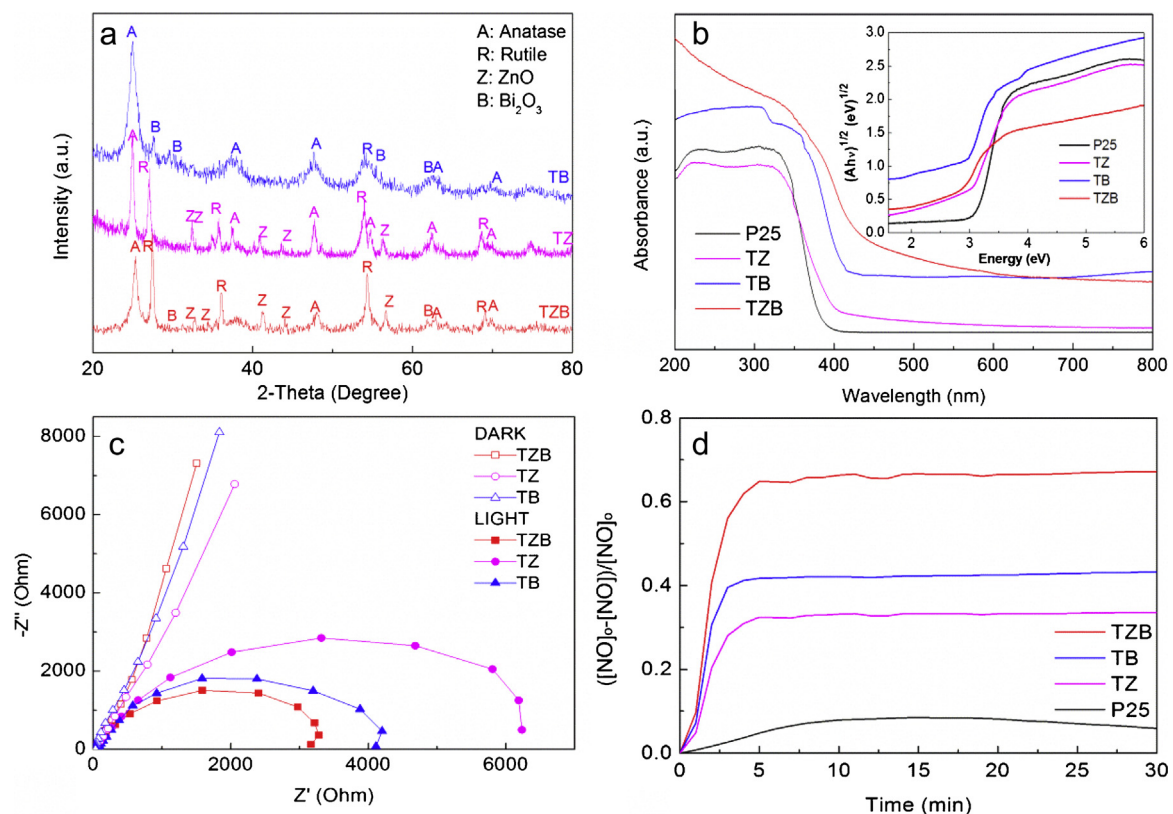


Fig. 8. (a) XRD pattern of TiO_2/ZnO (TZ) nanofibers, $\text{TiO}_2/\text{Bi}_2\text{O}_3$ (TB) nanofibers and TZB nanofibers prepared by the same method; (b) UV-vis absorption spectra of TZ, TB and TZB nanofibers (DRS presents in the insert); (c) EIS of TZ, TB and TZB nanofibers; (d) NO removal in the presence of TZ, TB and TZB nanofibers and P25 TiO_2 nanoparticles.

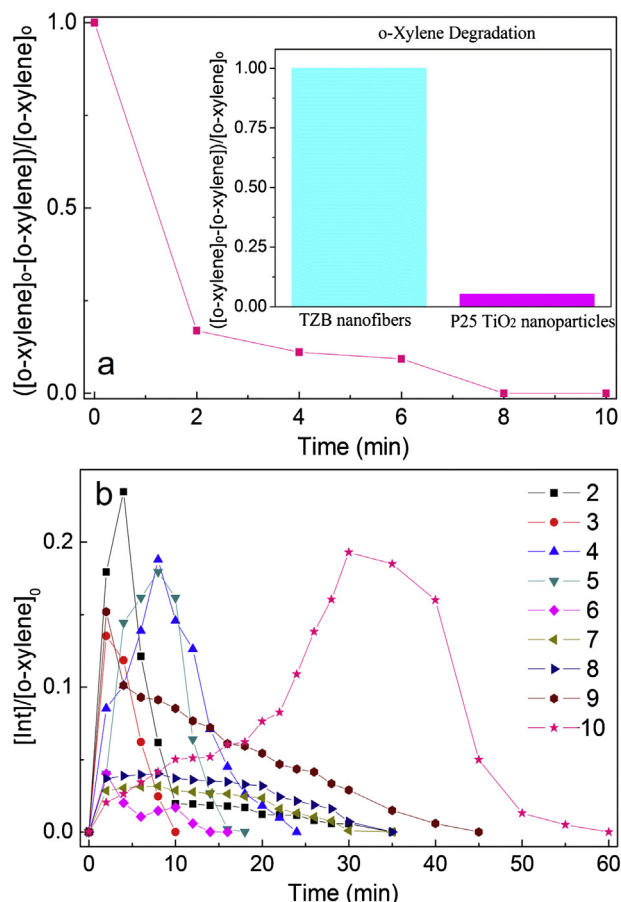


Fig. 9. (a) The relative variations of the *o*-xylene concentration against irradiation time in the presence of TZB nanofibers (Inset shows the benchmark test between TZB nanofibers and P25 nanoparticles with 10 min illumination); (b) The evolution profiles of *o*-xylene intermediates in the photocatalytic degradation process of TZB nanofibers.

of TZ, TB and TZB nanofibers are shown in Fig. 8b. The band gap energies of these three samples are determined to be 2.96, 2.62 and 2.51 eV, respectively. Due to the proper band position alignment, the band gap energies of TZ and TB are reduced due to synergistic effect. TZB has the lowest band gap energy due to the fact that it has the most heterojunctions. The EIS result (Fig. 8c) reveals that TB and TZ have lower impedences in dark condition and higher resistances under illumination, which implies more recombination and weaker charge transportation property when compared with TZB. The specific surface areas of TB, TZ and TZB nanofibers are determined respectively to be 51.2, 45.6 and 44.1 m²/g since the diameter of fibers increases gradually. The photocatalytic test result on the removal of NO by TB, TZ and TZB prepared by the same method together with commercial P25 TiO₂ nanoparticles is presented in Fig. 8d. TZB has the highest NO removal despite it has the least specific surface area among the three nanofiber samples. This superiority is attributed to improvement in band gap energies, recombination rates, and charge transport property.

3.5. Photocatalytic degradation of *o*-xylene

Taking into account photocatalytic theory and the synergistic effect among the four semiconductors, *o*-xylene was chosen as a representative volatile organic compounds (VOCs) pollutant to investigate the photocatalytic degradation process by TZB nanofibers and P25 TiO₂ nanoparticles (50 mg in each set of test) using full spectrum illumination. For 10 min illumination, the

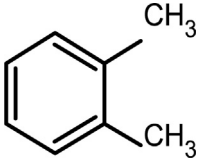
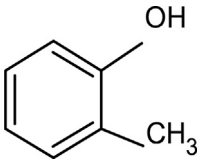
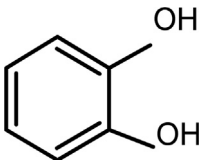
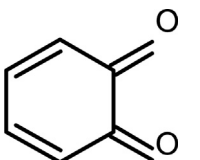
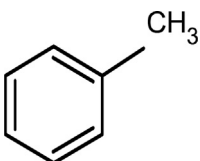
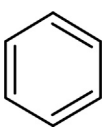
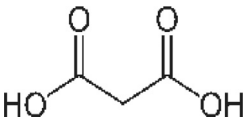
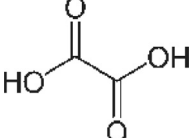
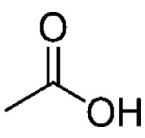
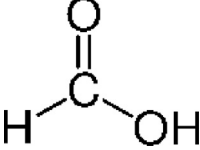
removal of *o*-xylene by commercial TiO₂ nanoparticles is very low (5.25%). In contrast, the removal by TZB nanofibers is up to 100%, which can be seen from Fig. 9a.

In order to gain a deeper insight into the *o*-xylene degradation by TZB nanofibers, the intermediates were identified and the evolution of major intermediates was investigated in each process. Nine intermediates (Compound 2–10) were identified according to different retention times in the GC spectrum during *o*-xylene degradation. The evolution profiles of *o*-xylene intermediates in the photocatalytic degradation process of TZB nanofibers are plotted in Fig. 9b.

The information on the intermediates including the mass of deprotonated ion ([M–H]⁺) of the daughter compounds, the proposed molecular structure, and the proposed fragments are summarized in Table 1.

Based on the intermediate products identified in the present system, the possible pathway for the photocatalytic degradation of *o*-xylene can be described as indicated in Fig. 10. The decomposition of *o*-xylene was initiated by the attack of •OH on the methyl group of the benzene ring, leading to the generation of compounds 2 and 3 at the first step. Upon further oxidation of •OH on the methyl group and the hydroxyl group on the benzene ring, compounds 4–6 were formed, respectively. The emergence of compound 10 was accompanied by the oxidation of methyl group at the beginning of the reaction. Compounds 7–10 were generated from the open-ring reaction. The final mineralization of these compounds lead to the formation of CO₂ and H₂O, which were too small size-wise to be detected in the experiment.

Table 1
Identified degradation products and their main fragments determined by GC–MS.

Compound	Retention time (min)	Molecular weight	Molecular ion and main fragments	Structural formula
<i>o</i> -xylene	26.818	106	106, 105, 91, 77, 51, 39	
2	29.016	108	108, 90, 77, 63, 51, 39, 27	
3	23.925	110	110, 92, 81, 63, 53, 39, 27	
4	21.142	108	108, 80, 73, 59, 54, 41	
5	22.764	92	91, 85, 73, 65, 51, 44, 39, 32	
6	19.184	78	78, 77, 63, 52, 39, 26, 15	
7	13.542	104	103, 57, 45, 33	
8	10.239	90	89, 61	
9	5.031	60	60, 45, 43, 29, 15,	
10	3.963	46	46, 45, 29, 17, 12	

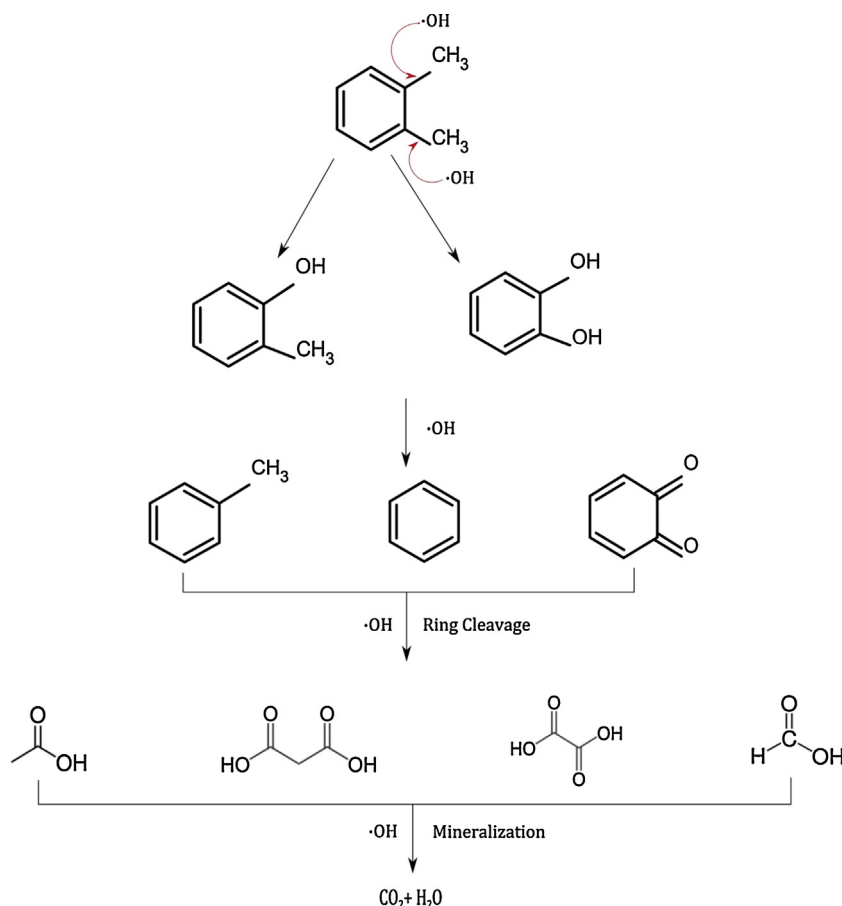


Fig. 10. Proposed photocatalytic degradation pathway of *o*-xylene in the present system.

4. Conclusions

$\text{TiO}_2/\text{ZnO}/\text{Bi}_2\text{O}_3$ composite nanofibers containing various Bi concentrations were synthesized by a sol-gel assist electrospinning method, followed by a heat treatment procedure at 650°C . The detailed morphology was characterized by SEM and TEM measurements. The as-synthesized composite nanofibers exhibited much higher photocatalytic activity for the oxidation of NO under simulated solar irradiation than commercial TiO_2 nanoparticles, and TiO_2/ZnO , $\text{TiO}_2/\text{Bi}_2\text{O}_3$ nanofibers prepared by the same method. The interlayers among these semiconductors were found to effectively separate photogenerated electron/hole pairs, as confirmed by the DRS and EIS measurements. The enhanced photocatalytic activity of TZB is attributed to the difference in the energy band positions of anatase, rutile, zincite and bismuth oxide. The energy diagram of the composited nanofibers resulted in a lower band gap energy level and reduced recombination rate due to greater charge separation. Moreover, the photocatalytic performances are more stable for the TZB nanofibers than that of TiO_2 nanoparticles, which can get deactivated easily. The degradation of *o*-xylene was also studied by GC/MS and a possible pathway was proposed based on the intermediates found.

A new kinetic model has been developed. Analysis of the photocatalysis data using the model revealed that at 0.2% Bi concentration, conversion of NO was limited by the flow rate and not by the kinetics of conversion. Further, the kinetic limitation is most likely due to chemical reaction in as much as physical diffusion and convection.

The effective $\text{TiO}_2/\text{ZnO}/\text{Bi}_2\text{O}_3$ composite nanofibers can offer a new generation of efficient photocatalytic material, benefiting environmental remediation and purification processes.

Acknowledgement

Carina Chun Pei thanks the Mechanical Engineering Department of The Hong Kong Polytechnic University for partial financial support for her PhD study.

Appendix A. Supplementary data

Supplementary data associated with this article can be found, in the online version, at <http://dx.doi.org/10.1016/j.apcatb.2015.03.021>.

References

- [1] L. Jing, B. Xin, F. Yuan, L. Xue, B. Wang, H. Fu, J. Phys. Chem. B 110 (2006) 17860–17865.
- [2] Y.-F. Zhu, L. Xu, J. Zhang, H.-Q. Qi, R.-G. Du, Y.-Z. Shao, C.-J. Lin, ECS Trans. 53 (2013) 31–39.
- [3] C. C.-y. Wang, Bottcher, D.W. Bahnemann, J.K. Dohrmann, J. Mater. Chem. 13 (2003) 2322–2329.
- [4] V. Štengl, S. Bakardjieva, N. Murafa, Mater. Chem. Phys. 114 (2009) 217–226.
- [5] D. Zhang, M. Wen, S. Zhang, P. Liu, W. Zhu, G. Li, H. Li, Appl. Catal. B: Environ. 147 (2014) 610–616.
- [6] D. Chen, Z. Jiang, J. Geng, Q. Wang, D. Yang, Ind. Eng. Chem. Res. 46 (2007) 2741–2746.
- [7] M. Sathish, B. Viswanathan, R.P. Viswanath, C.S. Gopinath, Chem. Mater. 17 (2005) 6349–6353.

- [8] Y. Cong, J. Zhang, F. Chen, M. Anpo, J. Phys. Chem. C 111 (2007) 6976–6982.
- [9] S. Bakardjieva, J. Šubrt, V. Štengl, M.J. Dianez, M.J. Sayagues, Appl. Catal. B: Environ. 58 (2005) 193–202.
- [10] T.A. Kandel, L. Robben, A. Alkaim, D. Bahnemann, Photochem. Photobiol. Sci. 12 (4) (2013) 602–609.
- [11] D. Tsukamoto, Y. Shiraishi, Y. Sugano, S. Ichikawa, S. Tanaka, T. Hirai, J. Am. Chem. Soc. 134 (2012) 6309–6315.
- [12] H. Chorfi, M. Saadoun, L. Bousselmi, B. Bessais, EPJ Web Conferences 29 (2012) 00015.
- [13] L. Wei, C. Shifu, Z. Sujuan, Z. Wei, Z. Huaye, Y. Xiaoling, J. Nanopar. Res. 12 (2010) 1355–1366.
- [14] Z. Liu, D.D. Sun, P. Guo, J.O. Leckie, Nano Lett. 7 (2006) 1081–1085.
- [15] L. Yang, W.W.-F. Leung, J. Wang, Nanoscale 5 (2013) 7493–7498.
- [16] A.M. Cant, F. Huang, X.L. Zhang, Y. Chen, Y.-B. Cheng, R. Amal, Nanoscale 6 (2014) 3875–3880.
- [17] Z. Bian, J. Zhu, S. Wang, Y. Cao, X. Qian, H. Li, J. Phys. Chem. C 112 (2008) 6258–6262.
- [18] Z. Zhao, J. Tian, D. Wang, X. Kang, Y. Sang, H. Liu, J. Wang, S. Chen, R.I. Boughton, H. Jiang, J. Mater. Chem. 22 (2012) 23395–23403.
- [19] S. Balachandran, M. Swaminathan, J. Phys. Chem. C 116 (2012) 26306–26312.
- [20] C.C. Pei, W.W.-F. Leung, Catal. Commun. 37 (2013) 100–104.
- [21] M. Yashima, D. Ishimura, K. Ohoyama, J. Am. Ceram. Soc. 88 (2005) 2332–2335.
- [22] A.A. Madhavan, A. Mohandas, A. Licciulli, K.P. Sanosh, P. Praveen, R. Jayakumar, S.V. Nair, A.S. Nair, A. Balakrishnan, RSC Adv. 3 (2013) 25312–25316.
- [23] P. Lommens, C. De Meyer, E. Bruneel, K. De Buysser, I. Van Driessche, S. Hoste, J. Eur. Ceram. Soc. 25 (2005) 3605–3610.
- [24] P. Du, L. Song, J. Xiong, C. Cui, Surf. Interface Anal. 45 (2013) 1878–1883.
- [25] C. Hu, X. Hu, L. Wang, J. Qu, A. Wang, Environ. Sci. Technol. 40 (2006) 7903–7907.
- [26] Q. Xiang, J. Yu, M. Jaroniec, J. Am. Chem. Soc. 134 (2012) 6575–6578.
- [27] F. Dong, Z. Wang, Y. Li, W.-K. Ho, S.C. Lee, Environ. Sci. Technol. 48 (2014) 10345–10353.
- [28] L.-j. Bai, G. Kou, Z.-y. Gong, Z.m. Zhao, Trans. Nonferrous Met. Soc. China 23 (2013) 3643–3649.
- [29] C. Ren, W. Qiu, H. Zhang, Z. He, Y. Chen, J. Mol. Catal. A: Chem. 398 (2015) 215–222.
- [30] F. Dong, Q. Li, Y. Sun, W.-K. Ho, ACS Catal. 4 (2014) 4341–4350.
- [31] M. Adachi, K. Noda, R. Tanino, J. Adachi, K. Tsuchiya, Y. Mori, F. Uchida, Chem. Lett. 40 (2011) 890–892.
- [32] Y. Hao, X. Yang, M. Zhou, J. Cong, X. Wang, A. Hagfeldt, L. Sun, ChemSusChem 4 (2011) 1601–1605.
- [33] H.N. Tsao, J. Burschka, C. Yi, F. Kessler, M.K. Nazeeruddin, M. Gratzel, Energy Environ. Sci. 4 (2011) 4921–4924.